JACS
JOURNAL OF THE AMERICAN CHEMICAL SOCIETY
pubs.acs.org/JACS
Article

Molecular Basis of the Electron Bifurcation Mechanism in the [FeFe]-Hydrogenase Complex HydABC

Alexander Katsyv,[§] Anuj Kumar,[§] Patricia Saura,[§] Maximilian C. Pöverlein, Sven A. Freibert, Sven T. Stripp, Surbhi Jain, Ana P. Gamiz-Hernandez, Ville R. I. Kaila,* Volker Müller,* and Jan M. Schuller*

Cite This: *J. Am. Chem. Soc.* 2023, 145, 5696–5709

Read Online

ACCESS | Metrics & More | Article Recommendations | Supporting Information

ABSTRACT: Electron bifurcation is a fundamental energy coupling mechanism widespread in microorganisms that thrive under anoxic conditions. These organisms employ hydrogen to reduce CO_2, but the molecular mechanisms have remained enigmatic. The key enzyme responsible for powering these thermodynamically challenging reactions is the electron-bifurcating [FeFe]-hydrogenase HydABC that reduces low-potential ferredoxins (Fd) by oxidizing hydrogen gas (H_2). By combining single-particle cryo-electron microscopy (cryoEM) under catalytic turnover conditions with site-directed mutagenesis experiments, functional studies, infrared spectroscopy, and molecular simulations, we show that HydABC from the acetogenic bacteria *Acetobacterium woodii* and *Thermoanaerobacter kivui* employ a single flavin mononucleotide (FMN) cofactor to establish electron transfer pathways to the NAD(P)$^+$ and Fd reduction sites by a mechanism that is fundamentally different from classical flavin-based electron bifurcation enzymes. By modulation of the NAD(P)$^+$ binding affinity via reduction of a nearby iron−sulfur cluster, HydABC switches between the exergonic NAD(P)$^+$ reduction and endergonic Fd reduction modes. Our combined findings suggest that the conformational dynamics establish a redox-driven kinetic gate that prevents the backflow of the electrons from the Fd reduction branch toward the FMN site, providing a basis for understanding general mechanistic principles of electron-bifurcating hydrogenases.

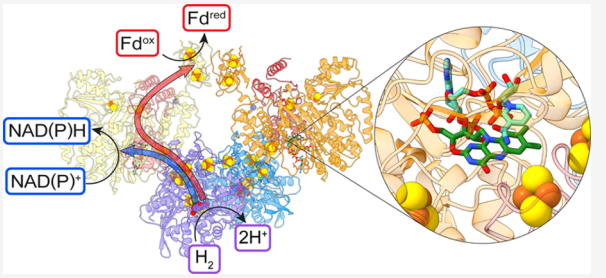

INTRODUCTION

Hydrogen cycling in anoxic ecosystems is essential for the complete breakdown of organic matter.[1] Hydrogen gas (H_2) is produced by fermentative bacteria from carbohydrates such as glucose, which is oxidized to acetate and CO_2.[2] During glycolysis, nicotinamide adenine dinucleotide (NAD^+) is reduced, but the formation of H_2 (E_0' = −420 mV) from NADH (E_0' = −320 mV) is thermodynamically restricted. Energy has to be invested to raise the potential of the electrons from NADH to the potential of molecular hydrogen. However, how this is mechanistically achieved has remained elusive for nearly a century until the discovery of the electron-bifurcating hydrogenase.[3−6] This soluble hydrogenase simultaneously uses reduced ferredoxin (Fd) (E_0' ≈ −450 mV) and NADH in proton (H^+) reduction and H_2 evolution and drives the endergonic electron transfer from NADH to H^+ by the exergonic electron transfer from reduced Fd to H^+.[3−5,7] Acetogenic bacteria, such as *Acetobacterium woodii*[5] and *Thermoanaerobacter kivui*,[7] have an electron-bifurcating [FeFe]-hydrogenase, HydABC, which produces H_2 during fermentation. However, the enzyme in acetogens generally operates in reverse and is also key for autotrophic growth on H_2 and CO_2, producing acetate by the Wood−Ljungdahl pathway.[8,9] The low-potential electron donor Fd is required for CO_2 reduction to carbon monoxide (CO), the precursor of the carbonyl group of acetate, and also for powering the ferredoxin/NAD^+ oxidoreductase (Rnf) and ferredoxin/H^+ oxidoreductase (Ech)−key respiratory enzymes in acetogens[9−12] that are essential for chemolithoautotrophic growth on H_2 and CO_2.[13] Thus, electron bifurcation is essential for the operation of the Wood−Ljungdahl pathway, often postulated to be one of the first metabolic pathways as it combines CO_2 fixation with the synthesis of ATP.[9,13,14]

These flavin-based electron bifurcation (FBEB) enzymes present a new unifying concept for energy coupling in anaerobic microbes.[9,14−16] To date, four classes of phylogenetically unrelated electron-bifurcating enzyme complexes are known:[17,18] the electron transfer flavoprotein (EtfAB) containing acyl-CoA dehydrogenases (e.g., butyryl-CoA dehydrogenase from *Clostridium kluyveri*[16] or caffeoyl-CoA reductase from *A. woodii*[19]); the NADH-dependent Fd/

Received: November 3, 2022
Published: February 22, 2023

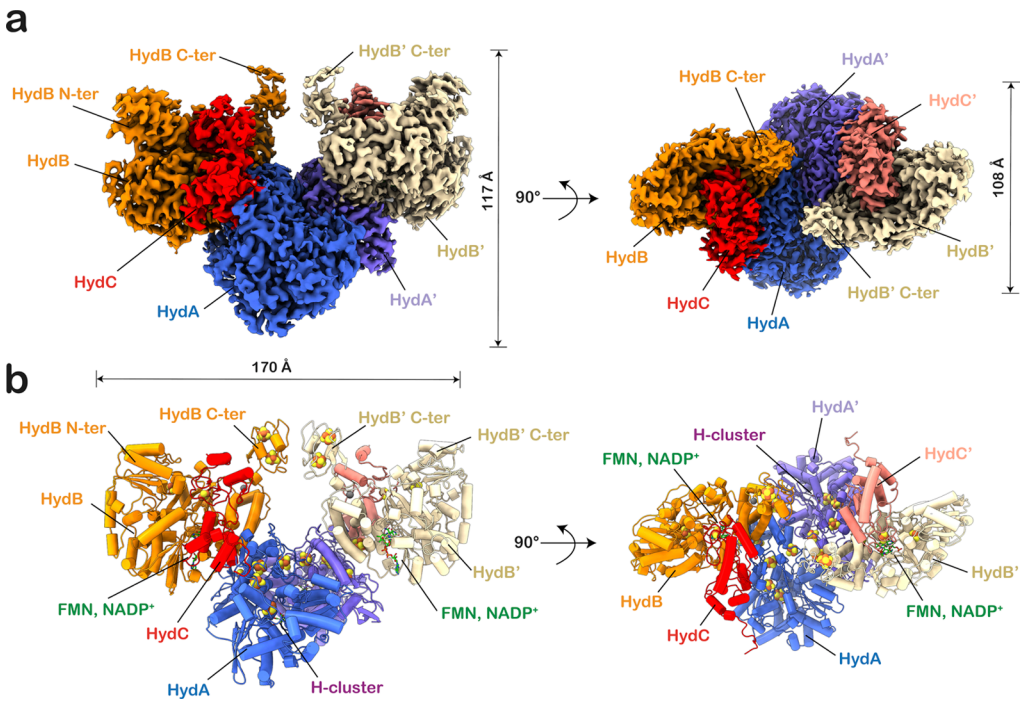

Figure 1. Molecular architecture of HydABC. (a) Three-dimensional segmented cryoEM density of the reduced $HydABC_{Tk}$ complex colored according to subunits. (b) Cartoon model of $HydABC_{Tk}$. HydA (blue/purple) contains the H-cluster along with four [4Fe−4S] and one [2Fe−2S] clusters; HydB (orange/yellow) contains FMN and $NAD(P)^+$ cofactors, including three [4Fe−4S] and two [2Fe−2S] clusters; HydC (red/salmon) harbors a single binuclear [2Fe−2S] cluster.

$NADP^+$ transhydrogenase (Nfn from *Thermotoga maritima*[20] or Stn from *Sporomusa ovata*[21]); the methanogenic hydrogenase/heterodisulfide reductase complex MvhADG−HdrABC;[22] and the [FeFe]-hydrogenases from *T. maritima*[3] or *A. woodii*.[5] In electron-bifurcating enzymes, two electrons originating from one donor such as NADH are split with one electron traveling energetically "downhill" to acceptors such as crotonyl-CoA[23] or heterodisulfides,[22,24] whereas the other electron is energetically pushed "uphill" to reduce Fd.[17] Structures of the first three groups have recently started to emerge—all contain a bifurcating flavin adenine dinucleotide whose fully reduced form is stabilized by a positively charged residue (Arg or Lys) near the isoalloxazine ring. The role and function of this bifurcating flavin in the electron-splitting process are now fairly well understood.[22,23,25−29] In contrast, the electron-bifurcating hydrogenase HydABC[3−5,7,30] does not have the classical bifurcating flavin, and thus, a different electron bifurcation mechanism has to apply.[30] Despite recent advances,[5−7,30] these enzymes remain poorly understood and their mechanistic principles have remained a major challenge.

To elucidate the molecular and functional basis of these electron-bifurcating hydrogenases, we study here HydABC from the acetogenic bacteria *A. woodii*[5] and *T. kivui*[7] which is a prototypical member of this unique enzyme class. HydABC from *A. woodii* ($HydABC_{Aw}$) employs NAD^+ as the nucleotide electron acceptor,[5] whereas the enzyme from *T. kivui* ($HydABC_{Tk}$) operates on $NADP^+$.[7] These differences reflect the natural electron carriers used in acetogens catalyzing the Wood−Ljungdahl pathway.[7] To address the mechanistic principles underlying the electron bifurcation process in this unique class of bifurcating enzymes, we combine biochemical assays with mutagenesis experiments, single-particle cryo-electron microscopy (cryoEM), infrared spectroscopy, and molecular simulations.

RESULTS

Structural and Functional Characterization of HydABC in Acetogens. The $HydABC_{Aw}$ complex was purified from *A. woodii* cell paste by chromatography as described before,[5] whereas, for $HydABC_{Tk}$, we took advantage of a recent plasmid-based production system introduced in *T. kivui* that allowed us to produce, purify, and engineer this isoform[7] (Figure S1a,b). Analytical size-exclusion chromatography (SEC) revealed that the complexes have a molecular mass of 306 kDa ($HydABC_{Aw}$) and 348 kDa ($HydABC_{Tk}$), which is consistent with HydABC being a homodimer of heterotrimers, $(HydABC)_2$ (Figure S1c). The purified HydABC complexes catalyze electron bifurcation from H_2 to Fd and $NAD(P)^+$ with an activity of 4.1 ± 0.7 U mg^{-1} (for $HydABC_{Aw}$) and 20.5 ± 2.8 U mg^{-1} (for $HydABC_{Tk}$), respectively (Figure S1e,f). Importantly, the H_2/Fd oxidoreductase activity was only detected upon the addition of pyridine nucleotides, demonstrating that Fd reduction is strictly dependent on $NAD(P)^+$ (Figure S1e,f) and verifying that the complexes show electron-bifurcating activity. Analysis of noncovalently bound cofactors using thin-layer chromatography (TLC) further revealed a FMN moiety as a part of the complexes (Figure S1d), consistent with previous results.[5] The metal cofactor content was analyzed by colorimetric methods[31] as well as inductively coupled plasma−mass spectrometry (ICP−MS), in which we detected iron (32 mol Fe and 39 mol Fe) and sulfur (30 mol S and 34 mol S) for $HydABC_{Aw}$[5] and $HydABC_{Tk}$,[7] as well as stoichiometric amounts of zinc (1.1 mol Zn and 1.0 mol Zn) as part of the complexes (Figures S3c and S5b).

To reveal the structural basis of the electron bifurcation process, we subjected the purified $HydABC_{Aw}$ and $HydABC_{Tk}$ complexes to single-particle cryoEM and collected data for (i) the oxidized and reduced states of $HydABC_{Aw}$ (Figures S2 and

https://doi.org/10.1021/jacs.2c11683
J. Am. Chem. Soc. 2023, 145, 5696−5709

S4) and (ii) for the oxidized and reduced state of HydABC$_{Tk}$ (Figure S5). The reduced states were obtained by preparing the cryoEM grids in a strictly anaerobic chamber with a gas composition of 95% N_2 and 5% H_2, that is, under catalytic turnover conditions, whereas the oxidized forms of the structures were obtained by preparing the cryoEM grids under aerobic conditions. The thermophilic complex from *T. kivui* showed higher stability, which allowed us to resolve the structure at a higher resolution (Figures 1, S5, and Movie S1), whereas the HydABC$_{Aw}$ complex could be captured in symmetric and asymmetric states (Figures S2−S4), reflecting the overall dynamics of the protein complex. Importantly, both the oxidized and reduced data sets showed the same overall molecular organization (Figures 1a,b, S3a,b, and S4g,h).

Already at the level of 2D class averages, it is apparent that HydABC$_{Aw}$ and HydABC$_{Tk}$ consist of a homodimer of heterotrimers (Figures S2 and S5), consistent with the SEC analysis (Figure S1c). The highest reconstructed map of HydABC$_{Tk}$ showed a resolution of 3.12 Å, with C_2 symmetry imposed, and containing all the cofactors (Figures 2, S5a, and Table S1). Moreover, while well-resolved at the symmetric core, external regions were less resolved, most likely due to their high mobility (Figure S5a), as also suggested by our MD simulations (see below). The HydABC$_{Aw}$ structures determined under aerobic conditions were resolved at 3.8 and 4.5 Å resolutions in conformations that provide insight into the alternative electron pathways (Figures S2, S3, and Table S1). Under anaerobic conditions, the HydABC$_{Aw}$ structure could be refined to a resolution of 3.4 Å harboring all the cofactors (Figure S4). We also determined the structure of HydABC$_{Tk}$ under aerobic conditions with a C_2 symmetry imposed with a resolution of 3.49 Å (Figure S5c), which exhibited greater stability than the HydABC$_{Aw}$ structure under aerobic conditions.

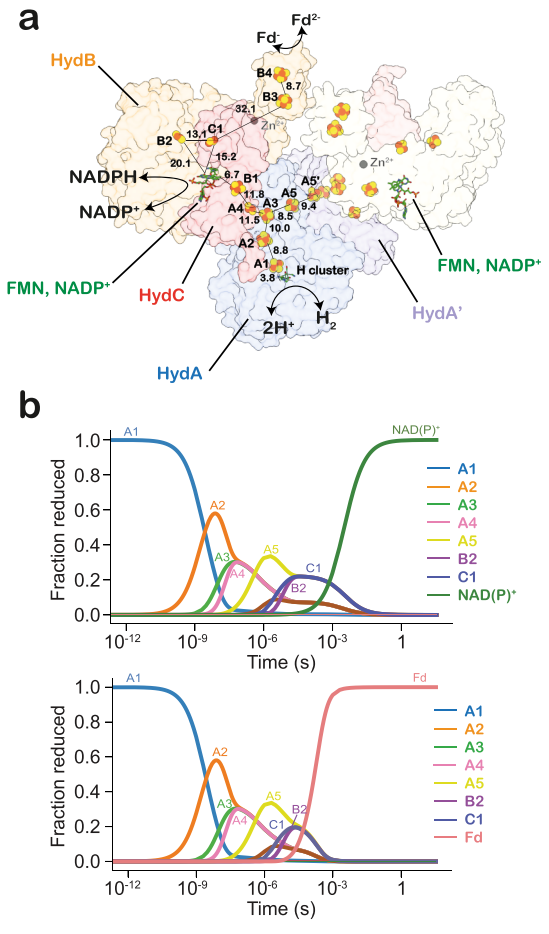

Figure 2. Cofactor organization of HydABC. (a) Overview of cofactor organization and the edge-to-edge distances in ångströms of HydABC$_{Tk}$. An electron path is indicated from the H-cluster in HydA to FMN in HydB. The reduction of $NADP^+$ takes place at FMN, and Fd is reduced at the C-terminus (C-ter) of HydB. (b) Modeled electron transfer kinetics from the H-cluster along the $NAD(P)^+$ (top) and Fd (bottom) edges predict electron transfer rates along the two branches/conformations in the millisecond timescale.

Based on the overall electron density (Figures S2−S5 and Table S1), we built fully intact structural models of the dimeric HydABC$_{Tk}$ (Figure 1) and HydABC$_{Aw}$ (Figure S3a,b,e) complexes. The resolved structures reveal that HydABC comprises two arms that lead from the active site [FeFe]-cofactor (the H-cluster) in HydA (HydA′), responsible for H_2 oxidation, to the nucleotide binding sites in HydB/C (HydB′/C′) (Figures 2a and S3e). These active sites are connected by five iron−sulfur clusters (Figures 2a and S3e) with edge-to-edge distances in the range of 6−12 Å, which can support rapid electron transfer between the H-cluster and the FMN/$NAD(P)^+$ binding site[32] (Figure 2b, see below). Interestingly, we observe density for a FMN molecule in our cryoEM structures of HydABC$_{Tk}$ and HydABC$_{Aw}$ resolved under aerobic conditions (Figures S3c and S5e) with no $NAD(P)^+$ bound, whereas, under reducing conditions, the structures show full occupancy of $NAD(P)^+$ on top of the FMN site (Figures 4a and S4j). This suggests that a single flavin is responsible for the dual function of electron bifurcation and $NAD(P)^+$ reduction, in contrast to other FBEB systems.

The electron density of the subunits HydA allowed us to identify four [4Fe−4S] clusters A1−A3 and A5, as well as a single [2Fe−2S] cluster A4 (Figures 2a, 3a, and S3e). A2−A4 serve as electron transfer clusters in the "F-domain" of HydA, whereas A1 of the "H-domain" is part of the active site (Figures 2a, 3b, S3e, and S4i). The [4Fe−4S] cluster A1 is coordinated by four cysteine residues, of which Cys354$_{Tk}$ (Cys356$_{Aw}$) additionally binds to the bimetallic iron core, ligated to two cyanide (CN^-) and three carbon monoxide (CO) ligands, as well as an aminodithiolate ligand (adt) (Figures 3b and S4i). The A1 cluster together with the di-iron core forms the active site "H-cluster", responsible for the oxidation of H_2 gas. Interestingly, in HydABC$_{Aw}$, one of the cysteine ligands of the A1 cluster (Cys299$_{Tk}$ in HydABC$_{Tk}$; Figure 3b) is replaced by a serine residue (Ser301$_{Aw}$; Figure S4i).

To probe the functional and spectroscopic features of the H-cluster, we next used in situ attenuated total reflection−Fourier transform infrared (ATR−FTIR) spectroscopy.[33] The ligands of the H-cluster give rise to a characteristic infrared absorbance between 2150 and 1750 cm^{-1}, which can be used as fingerprints of the redox state of [FeFe]-hydrogenases.[34] The "H_2−N_2" difference spectrum shows the conversion of the oxidized H_{ox} state (negative bands) into the one-electron reduced H_{red} species (positive bands) upon exchanging the gas atmosphere from N_2 to 10% H_2 (Figure 3c), with frequencies in good agreement with canonical [FeFe]-hydrogenases (Table S2). While the reduced H-clusters show a μCO ligand under cryogenic conditions (Figures 3b and S4i), our room-temperature FTIR data hints at three terminal CO ligands in H_{red} (Figure S6). This difference is explained by the

https://doi.org/10.1021/jacs.2c11683
J. Am. Chem. Soc. 2023, 145, 5696−5709

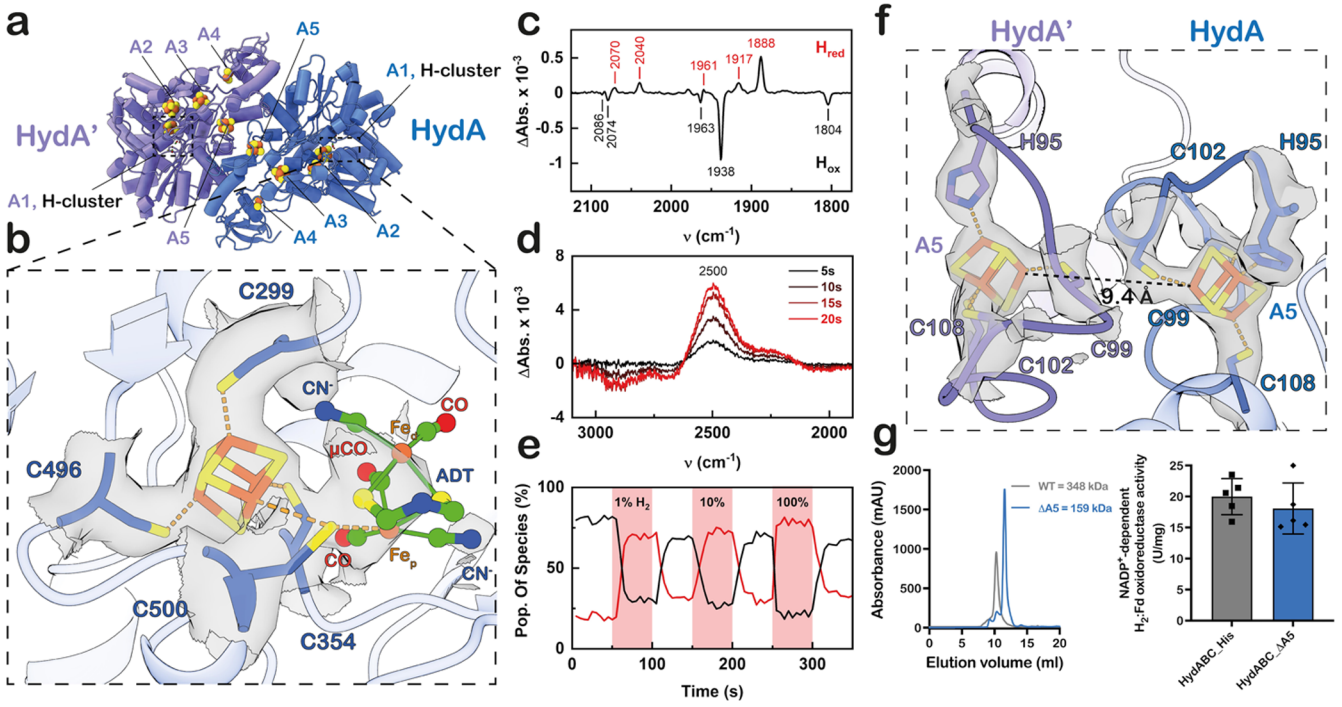

Figure 3. Biophysical and mutational analysis of $HydA_{Tk}$. (a) Dimerization architecture of HydAA′. (b) Close-up of the H-cluster along with the A1 [4Fe−4S] cluster superimposed with the EM density. Based on the spectroscopic signatures, the H-cluster resides in the one-electron reduced $H_{red}H^+$ state with a μCO ligand and open coordination site at the distal iron ion, Fe_d. The CN^- ligands were assigned according to potential hydrogen bonding partners. ADT refers to aminodithiolate. (c) "H_2−N_2" ATR-FTIR difference spectrum highlighting the accumulation of the reduced state H_{red} (positive bands) over H_{ox} (negative bands) upon H_2 oxidation. (d) When the same experiment is performed with D_2, the fast accumulation of HDO at 2500 cm^{-1} shows D_2 oxidation and the release of deuterium cations into the solvent. (e) Plotting the population of H_{ox} (black line) and H_{red} (red line) over time as a function of H_2 concentration (0−100%) highlights the reversibility of the redox conversion. (f) Close-up of the dimer interface showing the A5 and A5′ Fe/S cluster superimposed with the cryoEM density (in surface). (g) Analytical SEC of WT−$HydABC_{Tk}$ (MW = 348,000) and $HydABC_{Tk}$−ΔA5 (MW = 159,000). Electron bifurcation activity assay of WT−$HydABC_{Tk}$ and $HydABC_{Tk}$−ΔA5. For all data, the error bars show the standard deviation.

temperature-dependent equilibrium between H_{red} and its tautomer, $H_{red}H^+$.[35] We note that the residual electron density in the apical position of the distal iron ion (Fe_d) may hint at a water molecule[36] or another terminal ligand[37] in the structure of $HydABC_{Aw}$ (Figure S4i). To further link the difference spectra in Figure 3c to the oxidation of H_2, we repeated the experiment with "heavy hydrogen" ($^2H_2$), D_2. We observe a strong increase of a band at 2500 cm^{-1} (Figure 3d), which can be assigned to "semi-heavy water" (HDO) accumulating in the sample film when D_2 is oxidized and deuterium ions (D^+) combine with OH^- to form HDO.[33] In the presence of 1% CO, the H-cluster converts into a CO-inhibited H_{ox}−CO state,[37] whereas, at low pH, we observe the accumulation of the protonated oxidized $H_{ox}H$ state,[38−40] which further converts into the hydride state (H_{hyd})[41−43] upon reaction with H_2 (Figure S6). $HydABC_{Aw}$ showed similar infrared signatures and catalytic activities as $HydABC_{Tk}$ (Figure S6 and Table S2). Interestingly, the serine ligand of A1 in $HydABC_{Aw}$ has no apparent influence on the vibrational signature of the H-cluster (Figure S4i). Our spectroscopic analysis thus shows that the $HydABC_{Tk}$ and $HydABC_{Aw}$ are active complexes that carry a typical H-cluster and function as a bidirectional [FeFe]-hydrogenase (Figures 3b and S4i). Importantly, the reduction of HydABC under 1% H_2 is sufficient to ensure that the complex is reduced to the H_{red} state (Figure 3e), supporting that our cryoEM samples prepared under 5% H_2 reflect a reduced state of the complex.

HydABC Protomer Is the Minimal Functional Unit. Our resolved cryoEM structures of $HydABC_{Tk}$ and $HydABC_{Aw}$ show that the H-clusters in the respective protomers, HydA and HydA′, are connected via bridging [4Fe−4S] clusters A5 and A5′ (Figures 3f and S3c) (cf. also refs 6, 44 , 45). Although the short distance between these clusters could support electron transfer between the protomers (Figures 3f and S3e), their rare histidyl ligands will shift their redox potentials relative to the [2Fe−2S] center (A4) along the main chain.[46] Our kinetic simulations (Figures 2b and S7) indeed suggest that such redox shifts result in a higher electron flux along the main chain and block electron transfer across the dimer interface.

To experimentally probe the electron transfer activity across the interface, we deleted the A5 cluster by substituting the metal coordinating cysteine with glycines in $HydABC_{Tk}$ (Figure S8). The resulting ΔA5−$HydABC_{Tk}$ indeed migrated as a monomer in analytical SEC (Figures 3g and S8b), but the mutated complex showed undisturbed electron-bifurcating activity (Figure 3g and Table S3), validating that a single $HydABC_{Tk}$ protomer can catalyze the complete electron bifurcation reaction. This further supports that the same FMN cofactor is responsible for the reduction of both the $NAD(P)^+$ and Fd.

Molecular Organization of the HydBC Subcomplex. The structural core elements of HydB (residues 130−350 $HydB_{Aw}$; 160−380 $HydB_{Tk}$) and HydC are homologous to subunits Nqo1 and Nqo2 of the respiratory complex I[47]

https://doi.org/10.1021/jacs.2c11683
J. Am. Chem. Soc. 2023, 145, 5696−5709

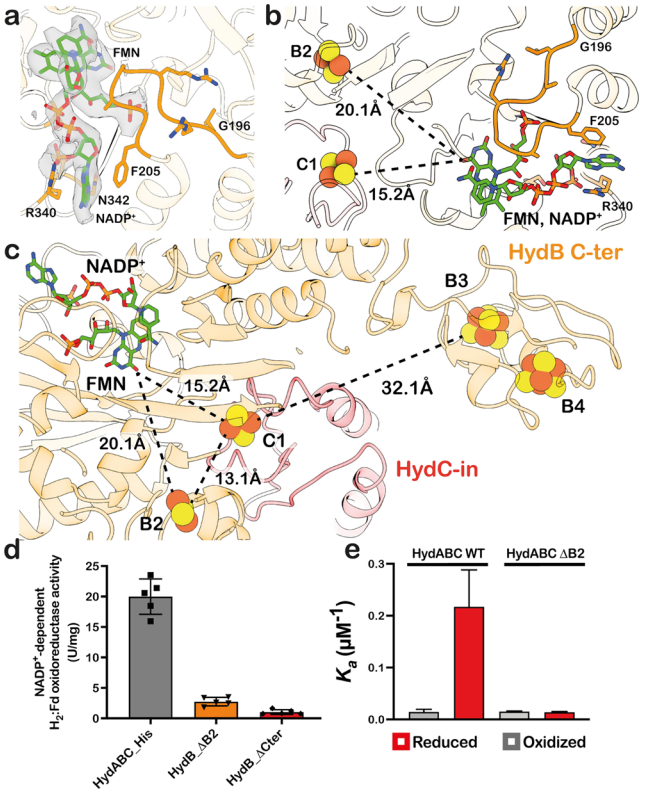

Figure 4. $NADP^+$ binding properties and mutational analysis of the HydBC core. (a) Close-up of the nucleotide binding site in $HydABC_{Tk}$, showing the cryoEM density around the $NADP^+$ and FMN cofactors. The nucleotides are stabilized by a Gly-rich loop (in orange) and interactions with Phe205 and Arg340. (b,c) Edge-to-edge distances from FMN to B2 and C1, as well as from C1 to B3 Fe/S centers in $HydABC_{Tk}$. (d) Electron bifurcation activity assay of different variants of $HydABC_{Tk}$. For all data, the error bars show the standard deviation. (e) Binding constant determined by MST of $NADP^+$ to $HydABC_{Tk}$–WT and $HydABC_{Tk}$–ΔB2. The variants had similar H_2: methylviologen-reducing activities as the wild-type enzyme (see Table S3). Experiments performed under reduced and oxidized states with $n = 3$ independent experiments.

(Figures S9, S10, and S18; see below), respectively. HydC consists of two domains, an N-terminal (N-ter) domain comprising a four-helical bundle domain, located in the vicinity of the HydB/HydA interface, and a C-terminal thioredoxin-like domain that carries the [2Fe–2S] cluster C1 (Figures 2a, 4c and S3).

The HydB core comprises a modified Rossmann fold with four (instead of six) β-sheets that noncovalently bind the FMN cofactor in a solvent-accessible cavity with a glycine-rich loop (Figures 4a,b, S4j, and S5e). Adjacent to the core domain and next to the HydA interface, we find another four-helical bundle domain that binds the [4Fe–4S] cluster B1 at around 6 Å distance from the FMN (Figures 2a and S3e). This cluster resembles the N3 [4Fe–4S] center of complex I that acts as an immediate electron acceptor from FMN in the latter (Figure S18).[48]

HydB also comprises a flexible N-terminal domain on the opposite side of the core region, with a thioredoxin-like [2Fe–2S] cluster B2, resembling the N1a cluster of complex I that has been suggested to enable electron bifurcation (Figures 2a, 4b,c, and S18).[48−50] The thioredoxin-like domains containing the B2 and C1 clusters are structurally highly similar and can be superimposed with an overall rmsd of ~1 Å (Figure S18). The C-terminus of HydB consists of a bacterial Fd-like domain with two [4Fe–4S] clusters, B3 and B4 (Figures 2a, 4c, and S3e), which shows structural similarity to the electron transferring flavoprotein, EtfAB.[27,51] This domain is connected to the four-helix bundle of the core region by an extended loop (residues 530–542 $HydB_{Aw}$; 561–573 $HydB_{Tk}$, Figure S9). The conserved Cys and His residues (Figure S10) located at this interface region further bind a Zn^{2+} ion as identified by ICP–MS, and as indicated by a strong density observed at this region (Figures S3c and S5b).

Conformational Changes in HydC Are Linked to the Oxidation State of the Protein. In the $HydABC_{Tk}$ structure prepared under reducing conditions (5% H_2), the HydC thioredoxin-like domain containing C1 forms a tightly bound, closed conformation (HydC-in) with the core domain of HydB (Figure 5d). However, we observe no direct electron transfer route from the B2/C1 clusters to B3/B4, located in the C-terminal domain of HydB that could form the Fd binding site (Figure 2a). In contrast, in the oxidized $HydABC_{Aw}$ structure, the density for the C-terminal HydC domain is not as strongly defined as compared to $HydABC_{Tk}$, indicating possible conformational changes. We therefore subclassified the data set and were able to isolate a class showing the C-terminal thioredoxin-like domain of HydC in an outward position (HydC-out) with the C1 cluster significantly closer to the B3/B4 clusters (ca. 15–18 Å as compared >25 Å in HydC-in; Figures 5d and S3d). Despite the somewhat lower resolution (4.5–4.3 Å), the secondary structures are visible and the domain can be accurately modeled. This observation is further corroborated by the fact that a similar conformation was also observed in the variance analysis of a related bifurcating [NiFe]-hydrogenase,[6] although a structural model of this state is missing. The HydC-out conformation leads to a rotation of HydC toward the B3 and B4 clusters, and an extended C1–FMN distance of >20 Å (Figures 5d and S11), whereas in the HydC-in state, the respective C1–FMN distance is around 13–17 Å (Figures 2a, 4b,c, S3e, and S11). Our kinetic simulations further support that the HydC-out conformation enables electron transfer to the B3 and B4 clusters (Figures 2b and S7b). It is thus tempting to speculate that the conformational changes of the HydC C-terminus could play a key step in the electron bifurcation mechanism of HydABC (Figures 5e and 6).

Reduction of an Iron–Sulfur Cluster as a Gating Element in Electron Bifurcation. In order to understand how HydBC switches between the $NAD(P)^+$ and Fd reduction modes, we performed molecular dynamics (MD) simulations in different putative states along the electron bifurcation cycle, using our cryoEM structures as a starting point [Figures 5, S11 and S12; see the Supporting Information (Extended Methods)]. The overall global dynamics of the HydABC dimer (modeled in the asymmetric NAD^+/apo state as well as the symmetric $NAD(P)^+/NAD(P)^+$ state) capture the local resolution inferred from the cryoEM maps (Figures S2, S4, S5, and S12) and support that our simulations sample the overall global motions of the enzyme (see also Movies S2, S3 and S4). Both HydABC isoforms are dynamically highly flexible, particularly around the C-terminal region of HydB, which forms several transient ion pairs with HydC. Based on edge-to-edge distances between the cofactors, extracted from the MD simulations of $HydABC_{Tk}$ and $HydABC_{Aw}$, our kinetic simulations suggest that the electrons could be transferred

https://doi.org/10.1021/jacs.2c11683
J. Am. Chem. Soc. 2023, 145, 5696–5709

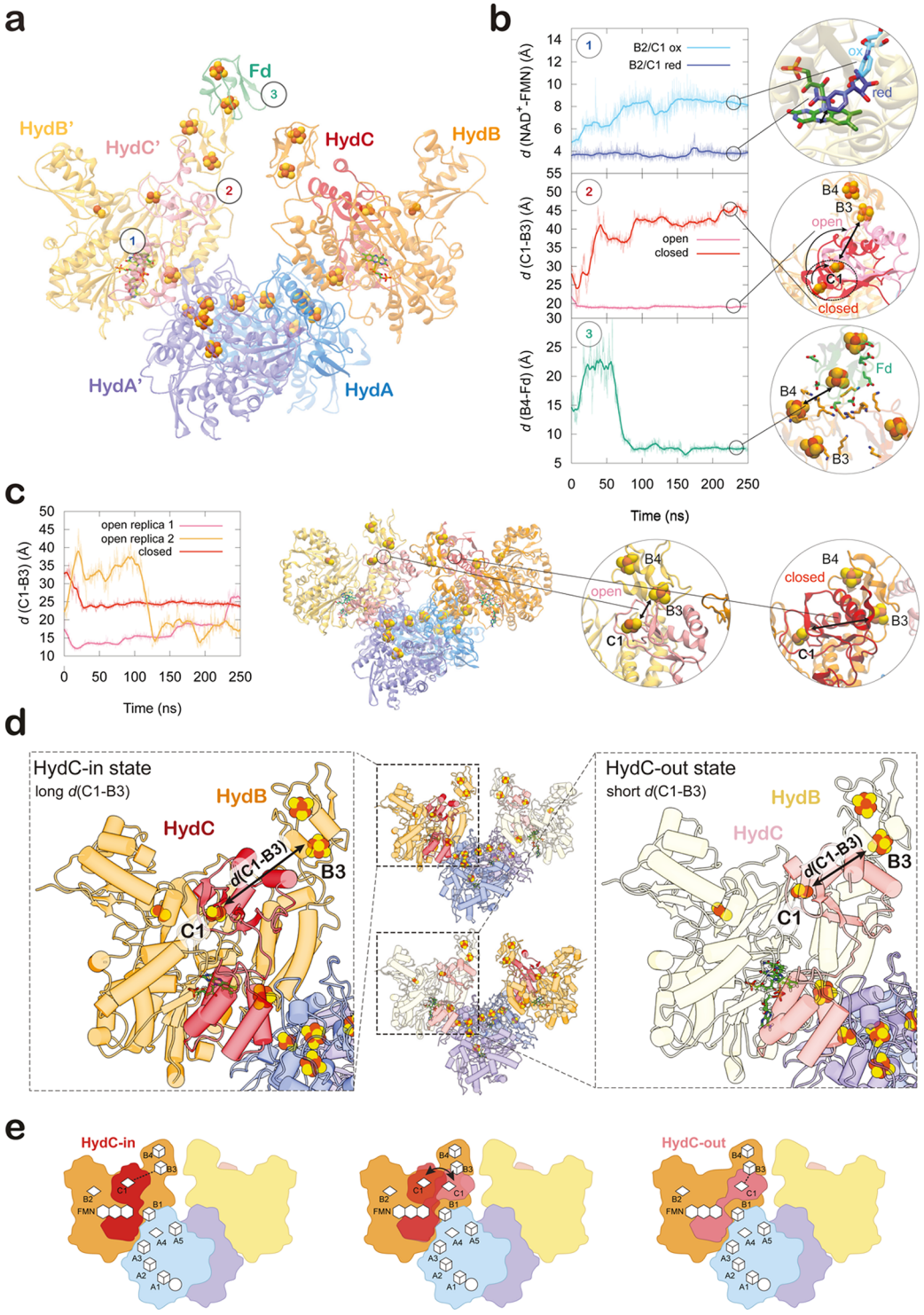

Figure 5. Molecular simulations of HydABC and HydC conformations. (a,b) Dynamics of $HydABC_{Aw}$ in different redox/conformational states. (a) Overall structure of the $HydABC_2$/Fd complex, highlighting the NAD^+/FMN site (1), the HydB/HydC interface (2), and the Fd binding site (3). (b) Distances between redox cofactors observed during MD simulations of $HydABC_{Aw}$: (1) reduction of B2 increases the affinity of NAD^+ (dark blue), whereas NAD^+ dissociates in the oxidized state (cyan). (2) C1−B3 distance in closed (red) and open (pink) conformations; (3) Fd binds at the top of the HydB C-terminal domain by electrostatic interactions, enabling rapid electron transfer between B4 and the Fd. (c) C1−B3 distance (open in pink/orange, closed in red) in simulations from $HydABC_{Tk}$. The HydC-out state of $HydABC_{Tk}$ (pink), generated based on the $HydABC_{Aw}$ [see the Supporting Information (Extended Methods)], remains in the open conformation for ca. 150 ns, after which it gradually switches to the closed state during the MD simulation. See Figure S11 for further MD simulations of $HydABC_{Tk}$, and Figure S17 for conformational changes linked to the ligand binding. (d) The asymmetric structure of $HydABC_{Aw}$ shows HydBC and HydB′C′ protomers in two different conformations: in the closed (HydC-in) state (left); the C1−B3 distance is too long for efficient electron transfer, whereas in the open (HydC-out) state (right), the HydC subunit moves toward the HydB C-ter domain bringing C1 and B3 closer, which would facilitate electron transfer toward the Fd branch. (e) Schematic representation of the closed (HydC-in) and open (HydC-out) states.

https://doi.org/10.1021/jacs.2c11683
J. Am. Chem. Soc. 2023, 145, 5696−5709

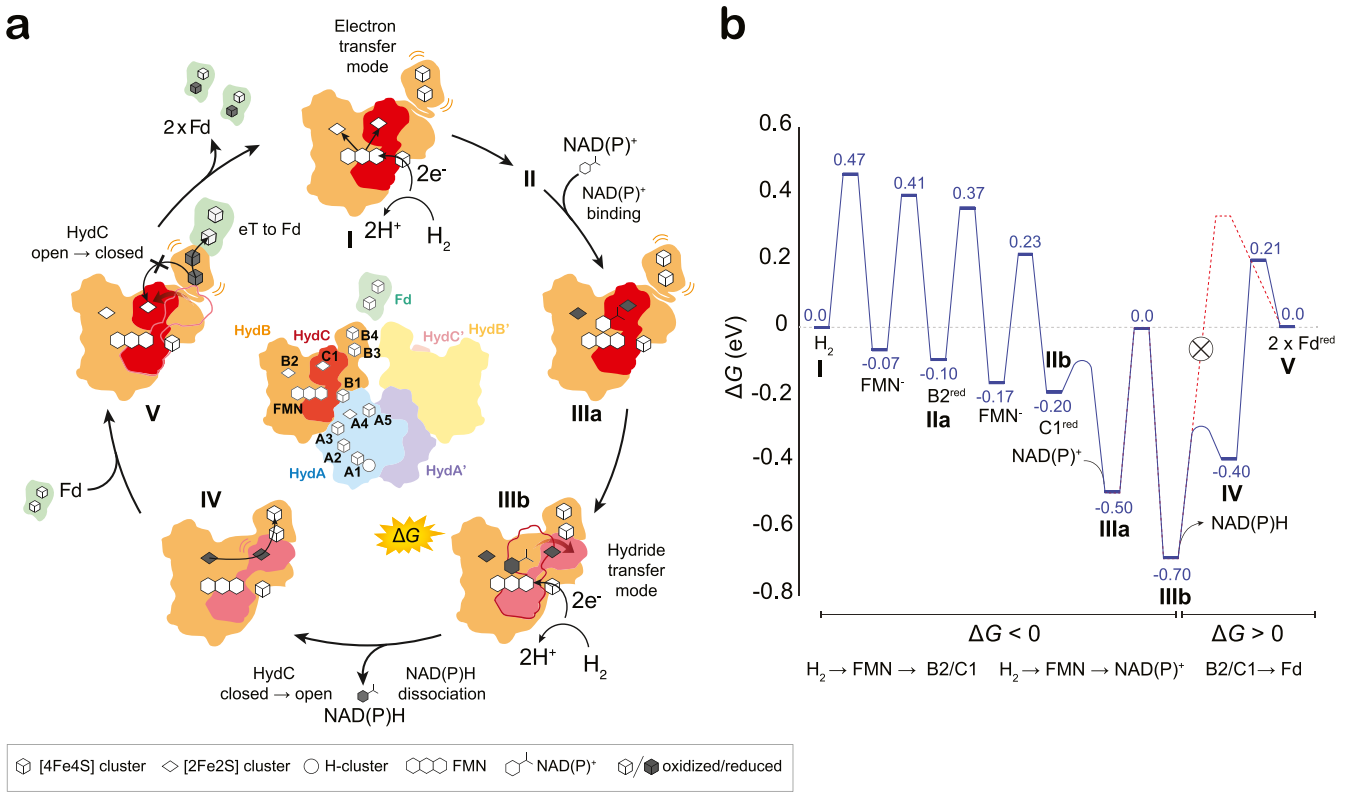

Figure 6. Proposed catalytic cycle of HydABC. (a) Putative electron bifurcation mechanism of HydABC (only the HydBC subunits are shown for simplicity). Oxidation of hydrogen gas by the H-cluster in the HydA subunit leads to the reduction of FMN and subsequent electron transfer to B2 and C1. Reduction of B2 increases the binding affinity of NAD(P)$^+$. Reduction of C1 triggers conformational changes in HydC that open toward the HydB C-ter domain. Another H_2 oxidation step leads to electron transfer to the nucleotide binding site, and the formation of NAD(P)H. Reduction and dissociation of the nucleotide decrease the C1−B3 distance, which allows for electron transfer to the HydB C-terminal (C-ter) domain. NAD(P)H dissociates and HydC transitions into a closed state that prevents electron backflow to the FMN site. Fd binding allows for electron transfer from the HydB C-ter domain, leading to oxidized HydABC, and reinitiation of a new catalytic cycle. (b) Derived free energy diagram of the putative catalytic cycle. See the Supporting Information (Extended Methods) for the derivation of the free energy profile.

from the H-cluster to FMN on millisecond timescales (Figures 2b and S7) and further from the FMN to the nearby B2 and C1 iron−sulfur clusters, located at around 15 Å edge-to-edge distances from the former in the closed state (HydC-in) protomer (Figures 2b and S7). Our model of the closed conformation of HydABC$_{Tk}$ also supports similar dynamics and distances between the HydB/C iron−sulfur clusters as the HydABC$_{Aw}$ system (Figures 5, S11, and S12). However, in stark contrast to the closed conformation, the open states (HydC-out) of both HydABC$_{Tk}$ and HydABC$_{Aw}$ samples FMN−C1/B2 distances >20 Å that are likely to block efficient electron transfer (Figure S11), and further support the conformational changes observed in the cryoEM maps.

In the nucleotide binding site, the modeled NAD(P)$^+$ moiety forms a stacking interaction with FMN that places the aromatic rings at around 4 Å from each other (Figures 4a, 5a,b, and S4j). Using quantum mechanical (QM) density functional theory (DFT) calculations performed based on the MD simulations [see the Supporting Information (Extended Methods)], we find that the hydride transfer between the nucleotides (FMNH$^-$/NAD$^+$ → FMN/NADH) has a modest energy barrier, which could support catalysis on physiologically relevant timescales (Figure S13a). Although we could not detect changes in the spectroscopic signatures of the flavin, our QM calculations, as well as simulations of the electron transfer kinetics, suggest that transient redox changes of the flavin could be involved during turnover.

Our MD simulations indicate that the reduction of the nearby B2 and C1 centers favors NAD$^+$ binding, whereas, in the oxidized state, we observed partial dissociation of the ligand from the binding site (Figures 5b and S11). These observations suggest that the nucleotide binding could occur after the reduction of the B2/C1 clusters (see below). Interestingly, we observe that the HydB loop (residues 197−206) samples different conformations in the apo and NAD$^+$/NADH bound states (Figure S17), further supporting conformational changes that could link to the electron bifurcation process.

To probe how the redox state modulates the nucleotide binding experimentally, we next tested the nucleotide binding affinity of the purified WT−HydABC$_{Tk}$ and ΔB2−HydABC$_{Tk}$ complexes prepared in different oxidation states. The truncated variant comprised all subunits, migrated similarly to the WT-dimer in SEC (Figure S8b), and had similar methyl viologen-reducing activities as the WT, but the activity of the ΔB2-variant in electron bifurcation is an order of magnitude lower as compared to the WT, which could result from the reduced NAD(P)$^+$ binding affinity (Figure 4d and Table S3). To determine the affinity of the complex for the nucleotide, we used microscale thermophoresis (MST), performed under strictly anaerobic conditions. The WT−HydABC$_{Tk}$ complex prepared under reducing conditions shows around 15 times higher affinity for NAD(P)$^+$ as compared to the oxidized complex (K_d = 4.6 and 69.6 μM, respectively; Figures 4e and

https://doi.org/10.1021/jacs.2c11683
J. Am. Chem. Soc. 2023, 145, 5696−5709

S14). In stark contrast, the affinity of $NAD(P)^+$ to ΔB2−$HydABC_{Tk}$ is independent of the oxidation state and comparable to that of the oxidized WT−$HydABC_{Tk}$ (K_d between 65 and 71 μM; Figures 4e and S14). These findings validate that the reduction of the B2 cluster indeed modulates the binding affinity of the $NAD(P)^+$, as predicted by our MD simulations. We can thus conclude that during the first step of the reaction cycle, two electrons can flow via the FMN cofactor to the B2/C1 clusters, whereas the reduction of the clusters themselves leads to a strong increase in nucleotide affinity. The FMN could then transfer the next two electrons as a hydride to the bound nucleotide, as suggested by our QM calculations (Figure S13a).

Our MD simulations further suggest that the reduction of the C1 cluster is involved in triggering the conformational change of HydC that moves toward the outward state (HydC-out) (Figure 5b,c). These conformational changes lead to a significantly shorter C1−B3 distance (Figure 5b,c) and could, in turn, allow for electron transfer toward the Fd branch. A similar HydC-out conformation is also captured in the MD simulations of $HydABC_{Tk}$, based on an asymmetric MD model of this isoform [Figure 5b,c, see the Supporting Information (Extended Methods)]. In the HydC-out state, the B2 and C1 clusters are within electron transfer distance from each other (see, e.g., simulations S5−S6 in Figure S11), which could support stepwise electron transfer toward B3, while the HydC-out conformation prevents the backflow of the electrons to the FMN (Figures 6 and S11). However, we note that the C1 cluster could also swing twice toward B2 to further support efficient electron transfer toward B3 along the low-potential branch. In the open conformation, the "outward" shifted C1 [2Fe−2S] cluster (see above) allows for the further reduction of the B3 and B4, trapping the electrons within this module, which may serve as a transient binding site for Fd (see below). Experimentally, we indeed observe low electron bifurcation activity in a HydABC complex with deleted C-terminus of the HydB, validating key functional aspects of the proposed electron transfer model along the Fd branch (Figure 4d and Table S3).

To probe the molecular principles underlying the Fd reduction process, we performed also MD simulations of the HydABC dimer with a bacterial Fd placed in the vicinity of HydB/C (see Materials and Methods, Table S5, and Figure 5a,b). These simulations suggest that Fd could dock to the C-terminal domain of HydB by electrostatic interactions between a Lys-rich loop ($Lys570-572_{Aw}$) and the anionic surface of the Fd (Figures 5a and S13b), similar to what has been suggested for the photosynthetic complex I[52−54] (Figure S13c) and other [FeFe]-hydrogenases.[55] The neighboring HydA′B′C′ arm stabilizes Fd by contacts with both the C-terminal domains of HydB and HydB′, indicating possible allosteric crosstalk. The explored conformations allow for electron transfer from B4 to the Fd at millisecond timescales (Figures 2b and S7), which completes the enzymatic cycle by reoxidation of all redox clusters and sets the enzyme for a new reaction cycle (Figure 6).

Putative Electron Bifurcation Mechanism in HydABC. Based on the combined findings, we derived a putative electron bifurcation model (Figure 6) to explain key features of the electron transfer along the high- and low-potential branches in HydABC. The cycle is initiated by the oxidation of H_2 (state I), which leads to the stepwise electron transfer from the H-cluster to B2 and C1 (state IIb), both of which are within electron transfer distance from the FMN in the HydC-in state (Figures 5 and 6).

The FMN in HydABC does not have an immediate residue that stabilizes the fully reduced flavin form, in contrast to other FBEB enzymes, which often have an Arg or Lys in the vicinity of the isoalloxazine ring of the flavin[20,22,23,25,27,29] (Figure S15), whereas we note that Asp232 could be involved in stabilizing the flavo-semiquinone form (Asp201_Aw/Asp232_Tk in Figure S17). The FMN in HydABC could thus function as a mediator in the electron transfer process, cycling through a transient one-electron reduced flavo-semiquinone state, as also suggested before.[44] Based on our estimates of the redox potentials, the two-electron reduced B2(red)/C1(red) state (IIb) is at a free energy level of ca. −0.2 eV (Figure 6b; see Supporting Information Extended Methods). Our MD simulations and MST experiments further suggest that the reductions of the nearby B2/C1 clusters significantly increase the affinity for $NAD(P)^+$, placing the nicotinamide bound form at a free energy level of ca. −0.5 eV, based on our experimentally determined K_d (Figures 4e, 6b, state IIIa; see Supporting Information Extended Methods). The bound cationic $NAD(P)^+$ now increases the redox potential of the flavin, which in turn could lead to the complete two-electron reduction to the $FMNH^-$ form, upon electron transfer from the H-cluster in a second H_2 oxidation step. Similar to complex I,[48] the $FMNH^-$ state further triggers a proton-coupled electron transfer to yield NAD(P)H, which we assign at −0.7 eV (state IIIb). The initial oxidation of two H_2 to form NAD(P)H and the reduced B2/C1 clusters thus provides the initial thermodynamic driving force for powering the uphill reduction of Fd (I → IIIb) in the endergonic electron transfer branch from B2/C1 to the Fd (IIIb → V) (Figure 6b; state IIIa; see Supporting Information Extended Methods). Interestingly, the highly stable, reduced NAD(P)H/B2(red)/C1(red) state (IIIb), as observed in the structure of $HydABC_{Aw}$/$HydABC_{Tk}$ under reducing conditions, is both thermodynamically ($\Delta G > +0.7$ eV) and kinetically (due to the long B2/C1−B3 distance) blocked from transferring the electrons onward to the Fd module, next to B3/B4 (Figure 6b; blocked red dashed line). However, we suggest that the dissociation of the reduced NAD(P)H triggers a conformational change from the closed to the open HydC conformation, as observed in the cryoEM structures of $HydABC_{Aw}$ under oxidizing conditions and in our MD simulations (Figure S11), and allowing for the efficient electron transfer from C1 to B3 (Figure 5c). This conformational change could be triggered, for example, via the $Asp201_{Aw}$/$Asp232_{Tk}$ loop, which changes orientation upon $NAD(P)^+$ binding and reduction (Figure S17) and is located next to the HydC subunit interface.

We estimate that this flipped open state IV is at around $\Delta G = -0.4$ eV, which would support the stepwise reduction of Fd (state V at $\Delta G = 0$ eV, Figure 6b). We note that the rapid relaxation of HydABC to its closed "ground" state, when the electron still resides within the B3/B4 module, favors the uphill Fd reduction and prevents electron back transfer to the flavin module. In this regard, our MD simulations suggest that the conformational switching back to closed conformation is favored by oxidation of the B2/C1 (Figures 6a and S11). Reoxidation of the clusters initiates a new reaction cycle upon further electron transfer from H_2. The derived free energy diagram (Figure 6b) also suggests that the overall reaction cycle at pH = 7 is thermodynamically highly restrained and that little energy can be lost in the form of dissipation.

https://doi.org/10.1021/jacs.2c11683
J. Am. Chem. Soc. 2023, 145, 5696−5709

The structure of a related electron-bifurcating [NiFe]-hydrogenase[6] supports general features of the described exergonic electron transfer branch, leading from the H-cluster to the NAD^+ reduction site but based on a variant of the general FBEB mechanism without the support of experimental data. Additionally, the C-terminal domain of HydB could not be resolved and is here suggested to modulate the electron transfer along the endergonic Fd branch, based on the combined structural, computational, and functional studies. Recently, Furlan and co-workers[44] also proposed that conformational changes in HydB could support bifurcation in the HydABC complex.

Our data suggest that HydABC employs kinetic gating principles achieved by conformational changes in the HydBC domain to transfer electrons along the high- and low-potential branches. In this regard, the proposed mechanism is fundamentally different from classical flavin-based electron-bifurcating enzymes, where high and low-potential electron acceptors are adjacent to the flavin. The difference lies in the affinity modulation of the binding nucleotides and in kinetic gating rather than in the formation of a stabilized flavo-semiquinone state. We suggest that the conformational changes at HydBC are thermodynamically driven by the reduction and dissociation of the nicotinamide.

Role of Protein Dynamics as a Gating Element in Electron Bifurcation. Based on our combined findings, we note that there are both fundamental similarities as well as differences between HydABC and other electron-bifurcating enzymes. As discussed above, several electron-bifurcating complexes employ a flavin, with crossed potentials to thermodynamically transfer electrons along spatially separated high- and low-potential pathways.[56] However, the importance of redox-driven conformational changes as an alternative to kinetically gate the electron transfer along the distinct pathways was also recognized early on. In this regard, complex III (cytochrome bc_1) in bacterial and mitochondrial respiratory chains achieves electron bifurcation via the mobile Rieske domain. Similar to the suggested [2Fe-2S] cluster motion in HydC, the [2Fe-2S] cluster of the Rieske domain in complex III employs a kinetically controlled bifurcation mechanism to achieve electron shuttling between the low-potential *b*-heme and the high-potential *c*-heme in the Q-cycle.[17,57,58] In this regard, the domain motion is also gated by the redox state of the Fe/S cluster and/or the redox state/character of the ligand.

Similar to HydABC, several types of electron bifurcation machinery have a modular structure that undergoes large-scale conformational changes. For example, the HdrABC bifurcation module of the methanogenic heterodisulfide reductase employs large-scale conformational changes in HdrA that mediate electron bifurcation.[24] Redox-triggered conformational changes have also been observed in EtfAB electron bifurcation modules. To this end, it was shown that rotation of the mobile EtfAB domain is central for the electron bifurcation process,[29] with similar conformational changes also proposed for the electron transferring flavoprotein complexes Bcd-EtfAB[26] and Fix/EtfABCX.[59] These findings generally suggest that redox-triggered conformational changes could establish central functional units in electron-bifurcating modules.[6,44]

CONCLUSIONS

We have here described the structure and function of HydABC from the acetogenic bacteria *A. woodii* and *T. kivui* and determined key molecular principles of its electron bifurcation mechanism by performing a series of cryoEM experiments in combination with biochemical functional assays, site-directed mutagenesis, and molecular simulations. This integrated approach allowed us to describe the HydABC complex under catalytic turnover conditions. In the H_2-reduced state, we observed a density for a bound $NAD(P)^+$ ligand, whereas, in the oxidized state, no $NAD(P)^+$ ligand could be resolved. We also observed a redox-triggered conformational change of the HydC domain comprising a [2Fe−2S] cluster, whereas our functional assays revealed that the electron bifurcation reaction is strictly $NAD(P)^+$-dependent and catalyzed within a single protomer of the dimeric HydABC. Based on simulations and experiments, we further showed that the FMN site switches between the exergonic $NAD(P)^+$ reduction and endergonic Fd reduction modes by modulation of the $NAD(P)^+$ binding affinity via reduction of the conserved B2 cluster. Based on the combined findings, we suggest that conformational dynamics of the HydBC unit establish a kinetic gate that prevents the backflow of the electrons from the Fd reduction branch toward the FMN site. Key to the bifurcation process is the unique iron−sulfur cluster environment around the FMN cofactor that is conserved in all members of the HydABC clade.[3−5,7,30] Importantly, the HydBC unit is utilized in a modular fashion as an electron input/output module in a variety of bioenergetic complexes that do not possess hydrogenase activity, but are linked either directly or via adapter modules, to other enzymatic activities important for anaerobic metabolism (Figure S18).[21,60] The proposed bifurcation mechanism could be generally conserved in electron-bifurcating hydrogenases of microbial respiratory chains and apply to all members of bifurcating complexes containing homologous HydBC domains.[21,60]

MATERIALS AND METHODS

Cell Growth. *A. woodii* (DSM 1030) was grown at 30 °C in the complex medium under anoxic conditions in 20 L flasks (Glasgerätebau Ochs; Bovenden-Lenglern, Germany) using 20 mM fructose as described previously.[61] *T. kivui* (DSM 2030) was grown at 66 °C in the complex medium under anoxic conditions in 1 L bottles (Glasgerätebau Ochs, Bovenden-Lenglern, Germany) using 28 mM D-glucose as the substrate.[62] The medium was prepared using the anaerobic techniques described previously.[63] Growth was monitored by measuring the OD at 600 nm. Plating and cultivation on solid media were performed as described in ref 64.

Purification of HydABC from *A. woodii* and His−HydABC from *T. kivui*. All buffers used were prepared using the anaerobic techniques described previously.[65] All purification steps were performed under strictly anaerobic conditions at room temperature in an anaerobic chamber (Coy Laboratory Products, Grass Lake, Michigan, USA) filled with 95−98% N_2 and 2−5% H_2. Cells of *A. woodii* were harvested and washed twice in buffer A (25 mM Tris/HCl, 20 mM $MgSO_4$, 2 mM DTE, 4 μM resazurin, 20% [v/v] glycerol, pH 7.6). The cells were resuspended in 30 mL of buffer A including 0.5 mM PMSF and 0.1 mg/mL DNAseI and passed one time through a French pressure cell (110 MPa). Cell debris was removed by centrifugation at 24,000*g*, 4 °C for 20 min. The membranes were removed by centrifugation at 130,000*g*, 4 °C, for 1 h. The supernatant contained the cytoplasm, which was further used to purify $HydABC_{Aw}$ as described previously.[5] For the purification of the His-tagged $HydABC_{Tk}$, *T. kivui pMU131_His-hydABC* cells were grown with 28 mM glucose as the carbon and energy source in the presence of 200 μg/mL kanamycin.[7] Cells were harvested and washed twice in buffer B (50 mM Tris/HCl, 150 mM NaCl, 20 mM $MgSO_4$, 10 mM imidazole, 0.5 mM DTE, 4 μM resazurin, 20% [v/v] glycerol, pH 7.5). The cells were resuspended in 20 mL buffer B including 0.5 mM PMSF and 0.1 mg/mL DNAseI and passed one time through a

https://doi.org/10.1021/jacs.2c11683
J. Am. Chem. Soc. 2023, 145, 5696−5709

French pressure cell (110 MPa). Cell debris was removed by centrifugation at 24,000*g* for 20 min. Purification of the His-tagged proteins was carried out on a nickel nitrilotriacetic acid (Ni^{2+}−NTA) resin (Qiagen, Hilden, Germany) using a gravity flow column under anoxic conditions as described previously.[7]

Cloning, Production, and Purification of His−HydABC$_{Tk}$ Variants. Nucleic acid exchanges in *hydABC* were introduced via site-directed mutagenesis using corresponding primers (Table S3). The plasmid *pMU131_His-hydABC*[7] was used as a template. Plasmids generated with nucleic acid exchanges in *hydA* are *pMU131_His-hydABCΔAN5* (C99G, C102G, and C108G), in *hydC* is *pMU131_-His-hydABCΔCN1* (C128A and C132G) and in *hydB* are *pMU131_His-hydABCΔBN2* (C82G and C86G) and *pMU131_His-hydABCΔBc-term* (P565-G630). Generated plasmids were checked by sequencing. A *T. kivui* Δ*hydAB* strain, lacking the genes *hydA* and *hydB*, was transformed with the verified plasmids, including *pMU131_His-hydABC* as described previously.[7] To verify the transformation, colonies were picked, and the transformed plasmids were checked using primer pairs seq1_for/seq2_rev (Table S4) binding on the *pMU131* backbone and amplifying the complete *His-hydABC* locus (Figure S8c). The purification of His−HydABC$_{Tk}$ variants was performed as mentioned above.

Enzyme Activity Assays. All enzyme assays, unless otherwise specified, were performed in 1.8 mL anoxic cuvettes (Glasgerätebau Ochs, Bovenden-Lenglern, Germany) sealed by rubber stoppers in an anoxic atmosphere at 66 °C at an overall liquid volume of 1 mL. All activity assays were performed in buffer C (50 mM EPPS, 10 mM NaCl, pH 8) as described previously.[5,7] One unit is defined as the transfer of 2 μmol electrons/min. $NAD(P)^+$/NAD(P)H was monitored spectrophotometrically at 340 nm (ε = 6.3 mM^{-1} cm^{-1}), ferredoxin (Fd; purified from *Clostridium pasteurianum*[66]) at 430 nm (ε = 13.1 mM^{-1} cm^{-1}), and benzyl viologen at 600 nm (ε = 12.0 mM^{-1} cm^{-1}).

Analytical Methods. The concentration of proteins was measured according to Bradford.[67] Proteins were separated in 12% polyacrylamide gels and stained with Coomassie brilliant blue G250. The molecular mass of the purified HydABC$_{Aw}$ and His−HydABC$_{Tk}$ was determined using a calibrated Superdex 200 column and defined size standards (ovalbumin: 43 kDa; albumin: 158 kDa; catalase: 232 kDa; ferritin: 440 kDa). The iron and sulfur content of the purified enzymes was determined by colorimetric methods.[31] The identity of bound flavin was elucidated by TLC.[7] The Zn^{2+} content was determined via ICP−MS.

1 μL HydABC$_{Aw}$ or HydABC$_{Tk}$ (100 μM) was analyzed by in situ ATR−FTIR spectroscopy as described previously.[33] The solution was dried and rehydrated under a N_2 aerosol, forming a reactive protein film that accumulated the oxidized state H_{ox} on the time scale of seconds ("auto-oxidation"). In the presence of 1−100% H_2, the one-electron reduced state H_{red} was accumulated. The conversion was mutually reversible, as observed for standard [FeFe]-hydrogenases.[68] The CO-inhibited state Hox−CO was enriched in the presence of 1% CO, which is a typical behavior of standard [FeFe]-hydrogenases.[69]

Microscale Thermophoresis Experiments. The His-tagged versions of WT−HydABC$_{Tk}$ and ΔB2 variants, 800 nM each, were labeled with 400 nM of Red-tris-NTA conjugated fluorophore (diluted in phosphate-buffered saline tween) in 50 mM TRIS pH 7.5, 150 mM NaCl, and 2 mM DTE. For experiments to measure affinities in the reduced state of the proteins, labeling and subsequent steps were performed under anoxic conditions inside an anaerobic chamber (Coy Laboratory Products, Grass Lake, Michigan, USA with a gas composition of 95% N_2 and 5% H_2). The labeled protein (100 nM final concentration) was titrated with a 13 (WT−HydABC$_{Tk}$) or 16 (ΔB2) step serial dilution of $NAD(P)^+$ with a starting concentration of 0.5 mM. The reaction mixtures were anaerobically transferred into glass capillaries and subsequently measured in a Monolith NT.115 outside the anaerobic chamber. Three independent measurements were performed at 50% laser and 75% LED power. For experiments measuring affinities under oxidizing conditions, the proteins were fluorescently labeled under oxic conditions. Thereafter, the protein samples were chemically oxidized using a final concentration of 40 μM of potassium ferricyanide. Measurements were carried out as described for anaerobic experiments except samples were under oxic conditions.

CryoEM Data Acquisition, Processing, and Model Building. For cryoEM data acquisition of HydABC$_{Aw}$ and HydABC$_{Tk}$ under oxidizing conditions, 3.5 μL of 1 mg/mL purified HydABC complex was used. Subsequently, it was rapidly applied to glow-discharged Quantifoil grids, blotted with force 4 for 3.5 s, and vitrified by directly plunging in liquid ethane (cooled by liquid nitrogen) using Vitrobot Mark III (Thermo Fisher) at 100% humidity and 4 °C. No $NAD(P)^+$ or Fd was added to the protein prior to vitrification. All nucleotides that were found in our structures were copurified with the enzyme. The automated data acquisition was performed using SerialEM software[70] on an FEI Titan Krios transmission electron microscope operated at 300 keV, equipped with a K3 Summit direct electron detector (Gatan). Due to the preferred orientation tilt movie frames at 20° were recorded at a nominal magnification of 22,500× with an electron dose of 55 e^- per $Å^2$ spread over 30 frames at a calibrated pixel size of 1.09 Å. A total of 3238 images were acquired. For HydABC$_{Tk}$, 1887 images were acquired with tilting and with an electron dose of 50 e^- per $Å^2$ spread over 50 frames at a calibrated pixel size of 1.09 Å.

The data set was processed using CryoSparc software.[71] The Dose-fractionated movies were gain-normalized, aligned, and dose-weighted using Patch Motion correction. The contrast transfer function (CTF) estimation was performed using Patch CTF estimation. Initially, 1000 particles were picked manually from 15 to 20 images which were then subsequently used to train a model to pick particles from the entire data set using the TOPAZ picker.[72] A total of 1,092,008 particles were extracted with a box size of 256 pixels. Using the SGD algorithm an ab initio model of 30 Å was created using 46,000 particles, which was further utilized to create two 3D reconstructions on entire particle images using homogeneous refinement. Both the 3D refinements were subsequently used for 3D classification using heterogeneous refinements. In the left branch, the best aligning 250,709 particles were subjected to nonuniform refinement with C2 symmetry for the 3D reconstruction of the dimeric HydABC complex with an overall resolution of 3.78 Å. In the right branch, the 2D cleaned particles were reprocessed in RELION 3.0.[73] After discarding suboptimal particles in a 3D classification run, the selected class was subjected to 3D autorefinement and 3D classification without alignment into six classes with a *T* value of 10. Two classes that showed the desired asymmetric features were combined and further refined in a final round of 3D autorefinement yielding 4.7 Å (gold standard FSC analysis of two independent half-sets at the 0.143 cutoff). The asymmetric 3D volume containing the particles was converted back into CryoSparc and the particles were extracted again, followed by nonuniform refinement, resulting in a resolution of 4.5 Å (4.3 Å tight mask). Using a similar strategy, the data for HydABC$_{Tk}$ was analyzed and h could be refined up to 3.49 Å with an imposed C_2 symmetry.

For the cryoEM data collection of HydABC$_{Tk}$ and HydABC$_{Aw}$ under reducing conditions, special care was taken to prevent any oxygen contact. Thus, all handling was carried out in an anaerobic glove box with a gas composition of 95% N_2 and 5% H_2 (a vitrobot was placed inside this anaerobic tent). Moreover, thanks to the controlled redox conditions, we can be sure that the entire protein complex is in a completely reduced state. For grid preparation, 4 μL of each protein at a concentration of 1 mg/mL was applied to glow-discharged Quantifoil grids, blotted for 4 s with force 5, and flash-frozen into liquid ethane using Vitrobot Mark IV (Thermo Fisher) at 100% humidity and 4 °C. Similar to the conditions used to determine the structure under an oxic state, no $NAD(P)^+$ or Fd was added to the protein before vitrification. The automated data collection was performed using SerialEM[70] on a JEOL CryoArm 200 microscope operated at 200 kV and equipped with a K2 direct electron detector. Frames were acquired at a magnification of 60,000× with a dose rate of 50 e^- per $Å^2$ which were fractionated into 50 frames at a calibrated pixel size of 0.84 Å. A total of 3018 and 1827 images were acquired for HydABC$_{Tk}$ and HydABC$_{Aw}$, respectively.

https://doi.org/10.1021/jacs.2c11683
J. Am. Chem. Soc. 2023, 145, 5696−5709

Both datasets were processed in CryoSparc, with a similar strategy as mentioned above. For both datasets, the frames were gain-normalized, aligned, dose-weighted using Patch Motion correction, and followed by CTF estimation. Manual picking of particles, followed by multiple rounds of topaz which resulted in "good" reference-free 2D classes that were further used for the processing. For $HydABC_{Tk}$, 193,719 particles were used for creating three ab initio classes, out of which only 150,493 particles exhibiting a nice ab initio model were used for the final round of NU-refinement. The refinement yielded 3D reconstructed maps for $HydABC_{Tk}$ with a resolution of 3.12 Å (C_2 symmetry) and 3.24 Å (C_1 symmetry). Both the maps were found to be identical, and thus, the map with the higher resolution was used for the model building and refinement. For $HydABC_{Aw}$, after 2D classification, 325,875 particles were cleaned by generating three ab initio classes. This resulted in 172,189 particles which were further refined to a resolution of 3.4 Å with no symmetry imposed.

Initial models of HydA, HydB, and HydC (from *T. kivui* and *A. woodii*) were generated separately from their protein sequences using AlphaFold[74] and thereupon fitted as rigid bodies into the density using UCSF Chimera.[75] The model was manually rebuilt using Coot[76] with information from all maps. Cofactors were placed manually and refined by using their respective CIF files. The final model was subjected to real-space refinements in PHENIX.[77] Illustrations of the models were prepared using UCSF Chimera,[75] UCSF ChimeraX,[78] and PyMOL.[79]

Molecular Simulations. To probe the functional dynamics of HydABC, we performed classical atomistic MD simulations of the $HydABC_{Aw}$ and $HydABC_{Tk}$, resolved in different conformational and redox states (Table S5). The dimeric cryoEM structural model of the HydABC complexes was embedded in a water box with 150 mM NaCl. The $HydABC_{Aw}$ system was modeled in the NADH and NAD^+ bound states, or without a bound nucleotide (*apo* state), whereas $HydABC_{Tk}$ was modeled with bound $NADP^+$ or NADPH. The Fe/S centers were modeled in the oxidized states or with the B2 and C1 clusters reduced. The H-cluster and the nearby [4Fe−4S] centers were parameterized based on DFT calculations at the B3LYP-D3/def2-SVP/def2-TZVP(Fe,S) level,[80−82] modeled with a hydride (H^-) ligand in the $Fe^{3+}Fe^{3+}$ state, while the A1 cluster was modeled in the oxidized state ($2Fe^{3+}2Fe^{2+}$) (Figures 3b, S4i, and S16). Force field parameters were derived from the molecular Hessian of the optimized model and charges from the restrained electrostatic potential procedure [see the Supporting Information (Extended Methods)]. The other Fe/S cofactors were adapted based on in-house models of respiratory complex I,[83−85] obtained at the same level of theory, while the CHARMM36[86] force field was used to model the protein, solvent, and ions. The Zn^{2+} site was modeled in HydB (Figures S3c and S5b) with parameters obtained from previous work on complex I.[83−85] The $HydABC_{Aw}$ simulations were also performed with Fd placed near the HydB/C interface, with the coordinates obtained from *Clostridium acidurici* Fd (PDB ID: 2FDN).[87] The two [4Fe−4S] centers of the Fd were modeled in an oxidized state. Additionally, simulations of a smaller $HydBC_{Aw}$ model were performed in the *apo*/NAD^+/NADH forms with different redox states for B2/C1 clusters. The $(HydABC)_2$/Fd system comprised ca. 502,000 atoms, the $(HydABC)_2$ systems 470,000 atoms, and the HydBC model 166,000 atoms (Figure S12d). The MD simulations were performed at 310 K using a 2 fs integration time step, 1 atm pressure, and by modeling the long-range electrostatics using the particle mesh Ewald approach. MD simulations were performed with NAMD2.14 and NAMD3.0.[88] Electron transfer kinetics was modeled using reorganization energies of λ = 0.7 eV, distance-dependent electronic couplings (with ρ = 0.76), and by assuming $E_{m,7}$ of −320 mV ([4Fe−4S]), −275 mV ([2Fe−2S]), −480 mV (H-cluster), and −520 mV for Fd based on biological electron transfer theory.[32] Kinetic simulations were carried out using COPASI.[89] Visual MD (VMD)[90] was used for visualization and analysis. See Table S5 for the list of all molecular simulations performed. Snapshots from the MD simulations are provided on Zenodo (access code: 10.5281/zenodo.6772075).

To probe the hydride transfer process between $FMNH^-$ and NAD^+, quantum chemical DFT models were built based on the NAD^+-bound structure (asymmetric model) of the HydB core domain. The models included the NAD^+ nicotinamide and ribose moieties, the FMN isoalloxazine ring and its ribityl unit, side chains (terminated at Cβ and saturated with hydrogen) of Asp201, Phe284, Asn192, Asn324, Ser429, as well as the backbone of residues Cys286−Glu289 (Figure S13a). The DFT models included 151 atoms, which were optimized at the B3LYP-D3/def2-SVP/ε = 4 level[80−82] in the reactant ($FMNH^-$/NAD^+), product (FMN/NADH), and transition state ($FMN\cdots H^-\cdots NAD^+$) with C$\beta$, C$\alpha$, and nucleotides C positions at the ribityl and ribose units fixed. Final energetics was evaluated at the B3LYP-D3/def2-TZVP/ε = 4 level. The DFT calculations were performed with TURBOMOLE v. 7.5.[91] See Supporting Information Extended Methods for further details of the molecular simulations.

■ ASSOCIATED CONTENT

Supporting Information

The Supporting Information is available free of charge at https://pubs.acs.org/doi/10.1021/jacs.2c11683.

$HydABC_{Tk}$ cryoEM density and atomic model (MP4)

Dynamics of $HydABC_{Aw}$ extracted from MD simulations (MP4)

Dynamics of $HydABC_{Aw}$-Fd extracted from MD simulations (MP4)

Dynamics of $HydABC_{Tk}$ extracted from MD simulations (MP4)

Extended methods, cryoEM data, biochemical assays, ATR−FTIR spectra, kinetic models, force field parameters, MD simulation data, DFT models, and structural analysis (PDF)

■ AUTHOR INFORMATION

Corresponding Authors

Ville R. I. Kaila − *Department of Biochemistry and Biophysics, Stockholm University, Stockholm 10691, Sweden;* orcid.org/0000-0003-4464-6324; Email: ville.kaila@dbb.su.se

Volker Müller − *Department of Molecular Microbiology & Bioenergetics, Institute of Molecular Biosciences, Johann Wolfgang Goethe University, Frankfurt am Main 60438, Germany;* orcid.org/0000-0001-7955-5508; Email: vmueller@bio.uni-frankfurt.de

Jan M. Schuller − *SYNMIKRO Research Center and Department of Chemistry, Philipps-University of Marburg, Marburg 35032, Germany*; Email: jan.schuller@synmikro.uni-marburg.de

Authors

Alexander Katsyv − *Department of Molecular Microbiology & Bioenergetics, Institute of Molecular Biosciences, Johann Wolfgang Goethe University, Frankfurt am Main 60438, Germany*

Anuj Kumar − *Department of Molecular Microbiology & Bioenergetics, Institute of Molecular Biosciences, Johann Wolfgang Goethe University, Frankfurt am Main 60438, Germany; SYNMIKRO Research Center and Department of Chemistry, Philipps-University of Marburg, Marburg 35032, Germany*

Patricia Saura − *Department of Biochemistry and Biophysics, Stockholm University, Stockholm 10691, Sweden*

Maximilian C. Pöverlein − *Department of Biochemistry and Biophysics, Stockholm University, Stockholm 10691, Sweden*

Sven A. Freibert − *Institut für Zytobiologie im Zentrum SYNMIKRO, Philipps-University of Marburg, Marburg 35032, Germany; Core Facility "Protein Biochemistry and Spectroscopy", Marburg 35032, Germany*

Sven T. Stripp − *Department of Physics, Experimental Molecular Biophysics, Freie Universität Berlin, Berlin 14195, Germany*

Surbhi Jain − *Department of Molecular Microbiology & Bioenergetics, Institute of Molecular Biosciences, Johann Wolfgang Goethe University, Frankfurt am Main 60438, Germany*

Ana P. Gamiz-Hernandez − *Department of Biochemistry and Biophysics, Stockholm University, Stockholm 10691, Sweden;* orcid.org/0000-0002-0961-328X

Complete contact information is available at: https://pubs.acs.org/10.1021/jacs.2c11683

Author Contributions

[§]A.Ka., A.Ku., and P.S. contributed equally. All authors have given approval to the final version of the manuscript.

Notes

The authors declare no competing financial interest.

CryoEM maps are available in the Electron Microscopy Data Bank; $HydABC_{Tk}$ reduced (15212), $HydABC_{Tk}$ oxidized (16011), $HydABC_{Aw}$ reduced (15166), $HydABC_{Aw}$ oxidized symmetric (13819), and $HydABC_{Aw}$ oxidized asymmetric (13818). The atomic models of $HydABC_{Aw}$ and $HydABC_{Tk}$ are available in the Protein Data Bank; $HydABC_{Tk}$ reduced (8A6T), $HydABC_{Tk}$ oxidized (8BEW), $HydABC_{Aw}$ reduced (8A5E), $HydABC_{Aw}$ oxidized symmetric (7Q4W), and $HydABC_{Aw}$ oxidized asymmetric (7Q4V). All models, force field parameters, simulation setups, and key trajectories have been deposited to the Zenodo database under: 10.5281/zenodo.6772075. Strains and plasmids generated in this study are available from the corresponding authors upon request.

■ ACKNOWLEDGMENTS

J.M.S. acknowledges the DFG for early career support through an Emmy Noether grant (SCHU 3364/1-1). We thank Jürgen Plitzko and Stefan Bohn for single-particle cryoEM data acquisition, and the cryoEM facility at University Marburg for data collection. This work received funding from the German Research Foundation (DFG) to V.M., the European Research Council under the European Union's Horizon 2020 research and innovation program/grant agreement 715311 (V.R.I.K.), the Knut and Alice Wallenberg Foundation (V.R.I.K. grant: 2019.0251), and the Swedish Research Council (V.R.I.K.). V.R.I.K. also acknowledges DFG for support within the Mercator Fellow Program to SFB1078. This work was also supported by the Swedish National Infrastructure for Computing (SNIC 2021/1-40 and SNIC 2022/1-29) at the Center for High Performance Computing (PDC) Center, partially funded by the Swedish Research Council through a grant agreement no. 2018-05973 and the Leibniz Rechenzentrum (LRZ, project:pr83ro), Germany.

■ REFERENCES

(1) Piche-Choquette, S.; Constant, P. Molecular hydrogen, a neglected key driver of soil biogeochemical processes. *Appl. Environ. Microbiol.* **2019**, *85*, No. e02418-18.

(2) Thauer, R. K.; Jungermann, K.; Decker, K. Energy conservation in chemotrophic anaerobic bacteria. *Bacteriol. Rev.* **1977**, *41*, 100−180.

(3) Schut, G. J.; Adams, M. W. The iron-hydrogenase of *Thermotoga maritima* utilizes ferredoxin and NADH synergistically: A new perspective on anaerobic hydrogen production. *J. Bacteriol.* **2009**, *191*, 4451−4457.

(4) Wang, S.; Huang, H.; Kahnt, J.; Thauer, R. K. A reversible electron-bifurcating ferredoxin- and NAD-dependent [FeFe]-hydrogenase (HydABC) in *Moorella thermoacetica*. *J. Bacteriol.* **2013**, *195*, 1267−1275.

(5) Schuchmann, K.; Müller, V. A bacterial electron bifurcating hydrogenase. *J. Biol. Chem.* **2012**, *287*, 31165−31171.

(6) Feng, X.; Schut, G. J.; Haja, D. K.; Adams, M. W. W.; Li, H. Structure and electron transfer pathways of an electron-bifurcating NiFe-hydrogenase. *Sci. Adv.* **2022**, *8*, No. eabm7546.

(7) Katsyv, A.; Jain, S.; Basen, M.; Müller, V. Electron carriers involved in autotrophic and heterotrophic acetogenesis in the thermophilic bacterium *Thermoanaerobacter kivui*. *Extremophiles* **2021**, *25*, 513−526.

(8) Wiechmann, A.; Ciurus, S.; Oswald, F.; Seiler, V. N.; Müller, V. It does not always take two to tango: "Syntrophy" via hydrogen cycling in one bacterial cell. *ISME J.* **2020**, *14*, 1561−1570.

(9) Müller, V.; Chowdhury, N. P.; Basen, M. Electron bifurcation: A long-hidden energy-coupling mechanism. *Annu. Rev. Microbiol.* **2018**, *72*, 331−353.

(10) Schoelmerich, M. C.; Müller, V. Energy conservation by a hydrogenase-dependent chemiosmotic mechanism in an ancient metabolic pathway. *Proc. Natl. Acad. Sci. U.S.A.* **2019**, *116*, 6329−6334.

(11) Katsyv, A.; Müller, V. A purified energy-converting hydrogenase from *Thermoanaerobacter kivui* demonstrates coupled H^+-translocation and reduction in vitro. *J. Biol. Chem.* **2022**, *298*, 102216.

(12) Wiechmann, A.; Trifunović, D.; Klein, S.; Müller, V. Homologous production, one-step purification, and proof of Na^+ transport by the Rnf complex from *Acetobacterium woodii*, a model for acetogenic conversion of C1 substrates to biofuels. *Biotechnol. Biofuels* **2020**, *13*, 208.

(13) Schuchmann, K.; Müller, V. Autotrophy at the thermodynamic limit of life: a model for energy conservation in acetogenic bacteria. *Nat. Rev. Microbiol.* **2014**, *12*, 809−821.

(14) Buckel, W.; Thauer, R. K. Flavin-based electron bifurcation, ferredoxin, flavodoxin, and anaerobic respiration with protons (Ech) or NAD^+ (Rnf) as electron acceptors: A historical review. *Front. Microbiol.* **2018**, *9*, 401.

(15) Herrmann, G.; Jayamani, E.; Mai, G.; Buckel, W. Energy conservation via electron-transferring flavoprotein in anaerobic bacteria. *J. Bacteriol.* **2008**, *190*, 784−791.

(16) Li, F.; et al. Coupled ferredoxin and crotonyl coenzyme A (CoA) reduction with NADH catalyzed by the butyryl-CoA dehydrogenase/Etf complex from *Clostridium kluyveri*. *J. Bacteriol.* **2008**, *190*, 843−850.

(17) Buckel, W.; Thauer, R. K. Flavin-based electron bifurcation, a new mechanism of biological energy coupling. *Chem. Rev.* **2018**, *118*, 3862−3886.

(18) Peters, J. W.; et al. A new era for electron bifurcation. *Curr. Opin. Chem. Biol.* **2018**, *47*, 32−38.

(19) Bertsch, J.; Parthasarathy, A.; Buckel, W.; Müller, V. An electron-bifurcating caffeyl-CoA reductase. *J. Biol. Chem.* **2013**, *288*, 11304−11311.

(20) Demmer, J. K.; et al. Insights into flavin-based electron bifurcation via the NADH-dependent reduced ferredoxin:$NADP^+$ oxidoreductase structure. *J. Biol. Chem.* **2015**, *290*, 21985−21995.

(21) Kremp, F.; Roth, J.; Müller, V. The *Sporomusa* type Nfn is a novel type of electron-bifurcating transhydrogenase that links the redox pools in acetogenic bacteria. *Sci. Rep.* **2020**, *10*, 14872.

(22) Wagner, T.; Koch, J.; Ermler, U.; Shima, S. Methanogenic heterodisulfide reductase (HdrABC-MvhAGD) uses two noncubane [4Fe-4S] clusters for reduction. *Science* **2017**, *357*, 699−703.

(23) Chowdhury, N. P.; et al. Studies on the mechanism of electron bifurcation catalyzed by electron transferring flavoprotein (Etf) and

butyryl-CoA dehydrogenase (Bcd) of *Acidaminococcus fermentans*. *J. Biol. Chem.* **2014**, *289*, 5145−5157.
(24) Watanabe, T.; et al. Three-megadalton complex of methanogenic electron-bifurcating and CO_2-fixing enzymes. *Science* **2021**, *373*, 1151−1156.
(25) Lubner, C. E.; et al. Mechanistic insights into energy conservation by flavin-based electron bifurcation. *Nat. Chem. Biol.* **2017**, *13*, 655−659.
(26) Demmer, J. K.; Pal Chowdhury, N.; Selmer, T.; Ermler, U.; Buckel, W. The semiquinone swing in the bifurcating electron transferring flavoprotein/butyryl-CoA dehydrogenase complex from *Clostridium difficile*. *Nat. Commun.* **2017**, *8*, 1577.
(27) Demmer, J. K.; et al. Molecular basis of the flavin-based electron-bifurcating caffeyl-CoA reductase reaction. *FEBS Lett.* **2018**, *592*, 332−342.
(28) Kaster, A. K.; Moll, J.; Parey, K.; Thauer, R. K. Coupling of ferredoxin and heterodisulfide reduction via electron bifurcation in hydrogenotrophic methanogenic archaea. *Proc. Natl. Acad. Sci. U.S.A.* **2011**, *108*, 2981−2986.
(29) Kayastha, K.; et al. Structure-based electron-confurcation mechanism of the Ldh-EtfAB complex. *Elife* **2022**, *11*, No. e77095.
(30) Schuchmann, K.; Chowdhury, N. P.; Müller, V. Complex multimeric [FeFe] hydrogenases: Biochemistry, physiology and new opportunities for the hydrogen economy. *Front. Microbiol.* **2018**, *9*, 2911.
(31) Fish, W. W. Rapid colorimetric micromethod for the quantitation of complexed iron in biological samples. *Methods Enzymol.* **1988**, *158*, 357−364.
(32) Page, C. C.; Moser, C. C.; Chen, X.; Dutton, P. L. Natural engineering principles of electron tunnelling in biological oxidation-reduction. *Nature* **1999**, *402*, 47−52.
(33) Stripp, S. T. In situ infrared spectroscopy for the analysis of gas-processing metalloenzymes. *ACS Catal.* **2021**, *11*, 7845−7862.
(34) Stripp, S. T. Bonds from bands. *Nat. Rev. Chem.* **2021**, *5*, 146−147.
(35) Stripp, S. T.; Mebs, S.; Haumann, M. Temperature dependence of structural dynamics at the catalytic cofactor of [FeFe]-hydrogenase. *Inorg. Chem.* **2020**, *59*, 16474−16488.
(36) Peters, J. W.; Lanzilotta, W. N.; Lemon, B. J.; Seefeldt, L. C. X-ray crystal structure of the Fe-only hydrogenase (Cpl) from *Clostridium pasteurianum* to 1.8 angstrom resolution. *Science* **1998**, *282*, 1853−1858.
(37) Senger, M.; et al. Stepwise isotope editing of [FeFe]-hydrogenases exposes cofactor dynamics. *Proc. Natl. Acad. Sci. U.S.A.* **2016**, *113*, 8454−8459.
(38) Senger, M.; et al. Protonation/reduction dynamics at the [4Fe-4S] cluster of the hydrogen-forming cofactor in [FeFe]-hydrogenases. *Phys. Chem. Chem. Phys.* **2018**, *20*, 3128−3140.
(39) Senger, M.; et al. Proton-coupled reduction of the catalytic [4Fe-4S] cluster in [FeFe]-hydrogenases. *Angew. Chem., Int. Ed. Engl.* **2017**, *56*, 16503−16506.
(40) Senger, M.; et al. Trapping an oxidized and protonated intermediate of the [FeFe]-hydrogenase cofactor under mildly reducing conditions. *Inorg. Chem.* **2022**, *61*, 10036−10042.
(41) Mulder, D. W.; Guo, Y.; Ratzloff, M. W.; King, P. W. Identification of a catalytic iron-hydride at the H-cluster of [FeFe]-hydrogenase. *J. Am. Chem. Soc.* **2017**, *139*, 83−86.
(42) Reijerse, E. J.; et al. Direct observation of an iron-bound terminal hydride in [FeFe]-hydrogenase by nuclear resonance vibrational spectroscopy. *J. Am. Chem. Soc.* **2017**, *139*, 4306−4309.
(43) Winkler, M.; et al. Accumulating the hydride state in the catalytic cycle of [FeFe]-hydrogenases. *Nat. Commun.* **2017**, *8*, 16115.
(44) Furlan, C.; et al. Structural insight on the mechanism of an electron-bifurcating [FeFe] hydrogenase. *Elife* **2022**, *11*, No. e79361.
(45) Schut, G. J.; et al. An abundant and diverse new family of electron bifurcating enzymes with a non-canonical catalytic mechanism. *Front. Microbiol.* **2022**, *13*, 946711.
(46) Artz, J. H.; et al. Reduction potentials of [FeFe]-hydrogenase accessory iron-sulfur clusters provide insights into the energetics of proton reduction catalysis. *J. Am. Chem. Soc.* **2017**, *139*, 9544−9550.
(47) Sazanov, L. A.; Hinchliffe, P. Structure of the hydrophilic domain of respiratory complex I from *Thermus thermophilus*. *Science* **2006**, *311*, 1430−1436.
(48) Saura, P.; Kaila, V. R. I. Energetics and dynamics of proton-coupled electron transfer in the NADH/FMN site of respiratory complex I. *J. Am. Chem. Soc.* **2019**, *141*, 5710−5719.
(49) Schulte, M.; et al. A mechanism to prevent production of reactive oxygen species by *Escherichia coli* respiratory complex I. *Nat. Commun.* **2019**, *10*, 2551.
(50) Verkhovskaya, M. L.; Belevich, N.; Euro, L.; Wikström, M.; Verkhovsky, M. I. Real-time electron transfer in respiratory complex I. *Proc. Natl. Acad. Sci. U.S.A.* **2008**, *105*, 3763−3767.
(51) Schut, G. J.; et al. The catalytic mechanism of electron-bifurcating electron transfer flavoproteins (ETFs) involves an intermediary complex with NAD^+. *J. Biol. Chem.* **2019**, *294*, 3271−3283.
(52) Schuller, J. M.; et al. Redox-coupled proton pumping drives carbon concentration in the photosynthetic complex I. *Nat. Commun.* **2020**, *11*, 494.
(53) Schuller, J. M.; et al. Structural adaptations of photosynthetic complex I enable ferredoxin-dependent electron transfer. *Science* **2019**, *363*, 257−260.
(54) Pan, X.; et al. Structural basis for electron transport mechanism of complex I-like photosynthetic NAD(P)H dehydrogenase. *Nat. Commun.* **2020**, *11*, 610.
(55) Winkler, M.; Kuhlgert, S.; Hippler, M.; Happe, T. Characterization of the key step for light-driven hydrogen evolution in green algae. *J. Biol. Chem.* **2009**, *284*, 36620−36627.
(56) Zhang, P.; Yuly, J. L.; Lubner, C. E.; Mulder, D. W.; King, P. W.; Peters, J. W.; Beratan, D. N. Electron bifurcation: thermodynamics and kinetics of two-electron brokering in biological redox chemistry. *Acc. Chem. Res.* **2017**, *50*, 2410−2417.
(57) Zhang, Z.; Huang, L.; Shulmeister, V. M.; Chi, Y. I.; Kim, K. K.; Hung, L. W.; Crofts, A. R.; Berry, E. A.; Kim, S. H. Electron transfer by domain movement in cytochrome bc_1. *Nature* **1998**, *392*, 677−684.
(58) Kaila, V. R. I.; Wikström, M. Architecture of bacterial respiratory chains. *Nat. Rev. Microbiol.* **2021**, *19*, 319−330.
(59) Feng, X.; Schut, G. J.; Lipscomb, G. L.; Li, H.; Adams, M. W. W. Cryoelectron microscopy structure and mechanism of the membrane-associated electron-bifurcating flavoprotein Fix/EtfABCX. *Proc. Natl. Acad. Sci. U.S.A.* **2021**, *118*, No. e2016978118.
(60) Wang, S.; Huang, H.; Kahnt, J.; Thauer, R. K. *Clostridium acidurici* electron-bifurcating formate dehydrogenase. *Appl. Environ. Microbiol.* **2013**, *79*, 6176−6179.
(61) Heise, R.; Müller, V.; Gottschalk, G. Sodium dependence of acetate formation by the acetogenic bacterium *Acetobacterium woodii*. *J. Bacteriol.* **1989**, *171*, 5473−5478.
(62) Leigh, J. A.; Mayer, F.; Wolfe, R. S. *Acetogenium kivui*, a new thermophilic hydrogen-oxidizing, acetogenic bacterium. *Arch. Microbiol.* **1981**, *129*, 275−280.
(63) Bryant, M. P. Commentary on the Hungate technique for culture of anaerobic bacteria. *Am. J. Clin. Nutr.* **1972**, *25*, 1324−1328.
(64) Basen, M.; Geiger, I.; Henke, L.; Müller, V. A genetic system for the thermophilic acetogenic bacterium *Thermoanaerobacter kivui*. *Appl. Environ. Microbiol.* **2018**, *84*, e02210−e02217.
(65) Hungate, R. E. Chapter IV A Roll Tube Method for Cultivation of Strict Anaerobes. *Methods in Microbiology*; Norris, J. R., Ribbons, D. W., Eds.; Academic Press, 1969; Vol. *3b*, pp 117−132.
(66) Schönheit, P.; Wäscher, C.; Thauer, R. K. A rapid procedure for the purification of ferredoxin from *Clostridia* using polyethylenimine. *FEBS Lett.* **1978**, *89*, 219−222.
(67) Bradford, M. M. A rapid and sensitive method for the quantification of microgram quantities of protein utilizing the principle of proteine-dye-binding. *Anal. Biochem.* **1976**, *72*, 248−254.

https://doi.org/10.1021/jacs.2c11683
J. Am. Chem. Soc. 2023, 145, 5696−5709

(68) Land, H.; Senger, M.; Berggren, G.; Stripp, S. T. Current state of [FeFe]-hydrogenase research: Biodiversity and spectroscopic investigations. *ACS Catal.* **2020**, *10*, 7069−7086.
(69) Duan, J.; et al. Geometry of the catalytic active site in [FeFe]-hydrogenase is determined by hydrogen bonding and proton transfer. *ACS Catal.* **2019**, *9*, 9140−9149.
(70) Schorb, M.; Haberbosch, I.; Hagen, W. J. H.; Schwab, Y.; Mastronarde, D. N. Software tools for automated transmission electron microscopy. *Nat. Methods* **2019**, *16*, 471−477.
(71) Punjani, A.; Rubinstein, J. L.; Fleet, D. J.; Brubaker, M. A. cryoSPARC: algorithms for rapid unsupervised cryo-EM structure determination. *Nat. Methods* **2017**, *14*, 290−296.
(72) Bepler, T.; et al. Positive-unlabeled convolutional neural networks for particle picking in cryo-electron micrographs. *Nat. Methods* **2019**, *16*, 1153−1160.
(73) Zivanov, J.; et al. New tools for automated high-resolution cryo-EM structure determination in RELION-3. *Elife* **2018**, *7*, No. e42166.
(74) Jumper, J.; et al. Highly accurate protein structure prediction with AlphaFold. *Nature* **2021**, *596*, 583−589.
(75) Pettersen, E. F.; et al. UCSF Chimera - A visualization system for exploratory research and analysis. *J. Comput. Chem.* **2004**, *25*, 1605−1612.
(76) Emsley, P.; Cowtan, K. Coot: model-building tools for molecular graphics. *Acta Crystallogr., Sect. D: Biol. Crystallogr.* **2004**, *60*, 2126−2132.
(77) Liebschner, D.; et al. Macromolecular structure determination using X-rays, neutrons and electrons: recent developments in Phenix. *Acta Crystallogr., Sect. D: Struct. Biol.* **2019**, *75*, 861−877.
(78) Goddard, T. D.; et al. UCSF ChimeraX: Meeting modern challenges in visualization and analysis. *Protein Sci.* **2018**, *27*, 14−25.
(79) Delano, W. L. *The PyMOL Molecular Graphics System*, version 2.3.4; Schrödinger LLC, 2002. http://www.pymol.sourceforge.net (accessed Nov 6, 2019).
(80) Schäfer, A.; Horn, H.; Ahlrichs, R. Fully optimized contracted Gaussian basis sets for atoms Li to Kr. *J. Chem. Phys.* **1988**, *97*, 2571−2577.
(81) Grimme, S.; Antony, J.; Ehrlich, S.; Krieg, H. A consistent and accurate ab initio parametrization of density functional dispersion correction (DFT-D) for the 94 elements H-Pu. *J. Chem. Phys.* **2010**, *132*, 154104.
(82) Becke, A. D. Density-functional thermochemistry. III. The role of exact exchange. *J. Chem. Phys.* **1993**, *98*, 5648−5652.
(83) Röpke, M.; Saura, P.; Riepl, D.; Pöverlein, M. C.; Kaila, V. R. I. Functional water wires catalyze long-range proton pumping in the mammalian respiratory complex I. *J. Am. Chem. Soc.* **2020**, *142*, 21758−21766.
(84) Röpke, M.; et al. Deactivation blocks proton pathways in the mitochondrial complex I. *Proc. Natl. Acad. Sci. U.S.A.* **2021**, *118*, No. e2019498118.
(85) Di Luca, A.; Gamiz-Hernandez, A. P.; Kaila, V. R. I. Symmetry-related proton transfer pathways in respiratory complex I. *Proc. Natl. Acad. Sci. U.S.A.* **2017**, *114*, E6314−E6321.
(86) Huang, J.; et al. CHARMM36m: an improved force field for folded and intrinsically disordered proteins. *Nat. Methods* **2017**, *14*, 71−73.
(87) Dauter, Z.; Wilson, K. S.; Sieker, L. C.; Meyer, J.; Moulis, J. M. Atomic resolution (0.94 A) structure of *Clostridium acidurici* ferredoxin. Detailed geometry of [4Fe-4S] clusters in a protein. *Biochemistry* **1997**, *36*, 16065−16073.
(88) Phillips, J. C.; et al. Scalable molecular dynamics on CPU and GPU architectures with NAMD. *J. Chem. Phys.* **2020**, *153*, 044130.
(89) Hoops, S.; et al. COPASI - A COmplex PAthway SImulator. *Bioinformatics* **2006**, *22*, 3067−3074.
(90) Humphrey, W.; Dalke, A.; Schulten, K. VMD: Visual molecular dynamics. *J. Mol. Graphics* **1996**, *14*, 33−38.
(91) Balasubramani, S. G.; et al. TURBOMOLE: Modular program suite for ab initio quantum-chemical and condensed-matter simulations. *J. Chem. Phys.* **2020**, *152*, 184107.

https://doi.org/10.1021/jacs.2c11683
J. Am. Chem. Soc. 2023, 145, 5696−5709